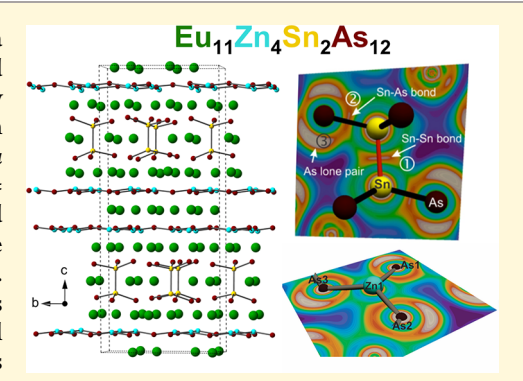


Eu₁₁Zn₄Sn₂As₁₂: A Ferromagnetic Zintl Semiconductor with a Layered Structure Featuring Extended Zn₄As₆ Sheets and Ethanelike Sn₂As₆ Units

Kasey P. Devlin,[†] Nasrin Kazem,[†] Julia V. Zaikina,^{†,§} Joya A. Cooley,[†] Jackson R. Badger,[†] James C. Fettinger,[†] Valentin Taufour,[‡] and Susan M. Kauzlarich*,[†]

ABSTRACT: We report the synthesis, structure, and magnetic properties of a new Zintl phase and structure type, Eu₁₁Zn₄Sn₂As₁₂. The structure and composition of this phase have been established by single-crystal X-ray diffraction and electron microprobe analysis. Eu₁₁Zn₄Sn₂As₁₂ crystallizes in monoclinic space group C2/c (No. 15) with the following lattice parameters: a= 7.5679(4) Å, b = 13.0883(6) Å, c = 31.305(2) Å, and $\beta = 94.8444(7)^{\circ}$ [$R_1 =$ 0.0398; $wR_2 = 0.0633$ (all data)]. The anisotropic structural features staggered ethane-like $[Sn_2As_6]^{12-}$ units and infinite ${}^2_{\infty}[Zn_2As_3]^{5-}$ sheets extended in the a-b plane. Eu cations fill the space between these anionic motifs. Temperature-dependent magnetic properties and magnetoresistance of this Zintl phase have been studied, and the electronic structure and chemical bonding were elucidated using first-principles quantum chemical calculations (TB-LMTO-ASA). Quantum chemical calculations show that the ethane-like



units can be considered as consisting of covalent single bonds; however, the $\frac{2}{\infty}[Zn_2As_3]^{5-}$ sheets are best described with delocalized bonding and there is evidence of Eu-As interactions. Temperature-dependent magnetization and transport properties between 2 and 300 K show a ferromagnetic transition at 15 K, a band gap of 0.04 eV, and negative colossal magnetoresistance.

■ INTRODUCTION

Compounds with layered crystal structures, 1,2 especially those containing arsenic and transition metals, have garnered considerable interest since the discovery of high-temperature superconductivity in $REO_{1-x}F_xFeAs$ (RE = rare earth metals) in which $SmO_{1-x}F_xFeAs$ holds the highest T_C of 58 K.^{3,4} Thereafter, numerous ternary and quaternary arsenide structures⁵ that show potential as superconductors under doping were synthesized; for example, Ba_{1-x}K_xFe₂As₂ shows a T_C of 38K.⁶ Besides their diverse crystal and electronic structures, pnictide-based Zintl phases are of interest because of various physical properties such as superconductivity, thermoelectricity, and colossal magnetoresistance that they exhibit.

Zintl compounds are a subset of intermetallics made of elements with different electronegativities. Zintl phase electron balance is realized by assuming the more electropositive elements donate electrons to the more electronegative elements to satisfy valence. Depending on the extent of the electron deficiencies of the electronegative elements and size effects, enormously diverse anionic networks are formed. 18,19

Zintl phases with a magnetic component can have interesting properties, as they are semiconductors in which the carrier concentration along with the identity of the

magnetic element, and therefore spin state, can be controlled. Control of composition through doping and/or defects^{20,21} is of interest for use in technology applications such as spintronics. Eu-containing Zintl phases that are magnetic semiconductors exhibit a large variety of magnetic properties, including colossal magnetoresistance (CMR). For example, compounds such as $Eu_{14}MnSb_{11}^{22}$ demonstrate multiple magnetic phase transitions, while Eu₂₁Cd₄Sb₁₈, Eu₂₁Zn₄Sb₁₈, and Eu₅Sn₂As₆ exhibit only one magnetic transition.²³⁻²⁵ Eucontaining layered structures can be even more magnetically diverse. Related layered structures, EuMgSn and EuZnSn, exhibit vastly different magnetic properties. EuMgSn has only one magnetic transition and exhibits magnetoresistance, and EuZnSn demonstrates metamagnetism. 26,22

As-containing layered structures, RECuZnAs₂ (RE = Ce-Nd, Sm, and Gd-Tm), typically exist as simple paramagnets.²⁸ Eu/As-containing layered structures continue to become more diverse. These layered phases can demonstrate anisotropic magnetic properties, such as EuIn₂As₂ and EuGa₂As₂. ^{16,29}

Received: June 29, 2018 Revised: September 20, 2018 Published: September 21, 2018

7067

[†]Department of Chemistry, University of California, One Shields Avenue, Davis, California 95616, United States [‡]Department of Physics, University of California, One Shields Avenue, Davis, California 95616, United States

Supporting Information

CMR materials exhibit a change in their electrical resistivity with the introduction of a magnetic field, coincident with a magnetic ordering temperature. While CMR has been reported in some Eu- and Eu/As-containing Zintl phases, ^{16,22,26,29,30} it is also not present in other Eu- and Eu/As-containing Zintl phases. ^{23–25,27,31,32} CMR is difficult to predict because the structural and electronic features for CMR have not been elucidated and may not be reported simply because MR was not measured. ³³

In this paper, a new transition metal arsenide-based layered Zintl compound, $\rm Eu_{11}Zn_4Sn_2As_{12}$, serendipitously synthesized via the Sn-flux route is reported. $\rm Eu_{11}Zn_4Sn_2As_{12}$ is a ferromagnetic semiconductor exhibiting CMR. The synthesis, structure, band structure calculations, and magnetic and transport properties are presented.

EXPERIMENTAL SECTION

Synthesis. In an attempt to make $Eu_{11}Zn_6As_{12}$ (with the $Sr_{11}Cd_6Sb_{12}$ structure type) using Sn-flux synthesis following the literature procedure,³⁴ the new phase of $Eu_{11}Zn_4Sn_2As_{12}$ was produced. Reaction conditions were optimized to yield Eu₁₁Zn₄Sn₂As₁₂ single crystals. All manipulations were carried out in argon- or nitrogen-filled gloveboxes or under vacuum to minimize oxidation. All starting elements were loaded in a 5 mL Canfield alumina crucible set³⁵ in the respective 11:6:12:95 Eu:Zn:As:Sn molar ratio to a total weight of 5 g (Eu element, Ames Laboratory, 99.999%; Zn powder, Alfa, 99.98%; As chips, Johnson Matthey Chemicals, 99.999%; and Sn shot, Alpha Aesar, 99.99%). The crucible set was placed into fused silica tubes and sealed under <100 mTorr of vacuum. The sealed tube was placed upright in a box furnace and heated at a rate of 200 °C/h to 650 °C, held for 1 h, and then heated at a rate of 200 °C/h to 875 °C. The reaction vessel was immediately cooled to 800 °C and held for 1 h. The reaction vessel was slowly cooled at a rate of 2 °C/h to 500 °C. Once at 500 °C, the sample was heated at a rate of 200 °C/h to 650 °C, at which point molten tin was removed by centrifugation. Finally, silver-colored, reflective block-like crystals of Eu₁₁Zn₄Sn₂As₁₂ were observed as the product by opening the reaction vessel in a N₂-filled glovebox equipped with an optical microscope and at moisture levels of <1 ppm. The optimized synthesis results in crystals of Eu₁₁Zn₄Sn₂As₁₂, EuZn₂As₂, and Eu₅Sn₂As₆. The presence of these three phases was confirmed via unit cell determination of single crystals. The crystals were separated by morphology. The large crystals were Eu₁₁Zn₄Sn₂As₁₂, and the remaining small crystals were a mixture of EuZn₂As₂ and Eu₅Sn₂As₆.

Single-Crystal X-ray Diffraction. Single-crystal X-ray diffraction (XRD) data were collected from the silver reflective needle-like crystal with a size of 0.0875 mm \times 0.0375 mm \times 0.025 mm at 89 K using an APEX II X-ray diffractometer (Bruker AXS) with a CCD detector, Mo $K\alpha$ radiation, and a graphite monochromator. More than 10 other single crystals were selected for unit cell determination and exhibited the same unit cell metric. The initial unit cell determinations were performed by using 1802 reflections from 200 frames with $I/\sigma = 2$. The only highest-symmetry Bravais lattice suggested for the refined unit cell parameters was a C-monoclinic unit cell with the following dimensions: a = 7.58 Å, b = 13.13 Å, c = 31.38 Å, and $\beta = 94.84^{\circ}$. The frames were integrated by using SAINT program within APEX II version 2011.4-1. Centrosymmetric space group C2/c (No. 15) was suggested by XPREP based on the analysis of systematic absences. The structure was determined using direct methods, and difference Fourier synthesis was used to assign the remaining atoms (SHELXTL version 6.14).36 Atomic coordinates were standardized with STRUCTURE TIDY.³⁷ Three different crystals were analyzed because of a problem with a large residual peak along the Sn-Sn bond. Regardless of the crystal size, the residual peak was persistent. It was best modeled as a stacking perturbation, where a Eu atom is replacing the Sn-Sn pair, so that the Eu position is located at the center of the Sn-Sn bond. In turn, the Sn-Sn pair is replacing a neighboring Eu site. This minor perturbation has been observed in

multiple crystals occurring at \sim 2% in each crystal. Upon analysis of the occupancy of the crystallographic sites, the Sn site was found to be partially occupied (\sim 98.5%), while the rest of the sites were refined to be fully occupied. The Sn site can be considered fully occupied when considering the stacking perturbation. The CIF is provided in the Supporting Information.

Powder X-ray Diffraction. Powder X-ray diffraction (PXRD) was performed on ground powders, made from the reaction products of the Sn-flux reactions, loaded onto a zero-background holder. PXRD was collected with a Bruker D8 Eco Advance Powder X-ray diffractometer with Cu $K\alpha$ radiation ($\lambda = 1.54060$ Å) with a 2θ range from 10° to 80° with a step size of $\sim 0.02^\circ$ and a scan rate of 1 s/step utilizing a Lynx-EX detector. Sn-flux reaction products were ground and plated, and the diffraction pattern was collected on days 0, 1, 3, 8, 13, and 20. The peaks from the bulk reaction product were identified via peak matching as Eu₁₁Zn₄Sn₂As₁₂, EuZn₂As₂, Eu₅As₄, Sn, and an unidentified phase. Eu₅Sn₂As₆ was not identified via peak matching, but single crystals were confirmed via unit cell determination prior to grinding. The Eu₁₁Zn₄Sn₂As₁₂ phase was found to be air stable beyond 20 days (Figure S1).

Electron Microprobe Analysis (EMPA). Single crystalline samples were enclosed in epoxy and polished to provide flat surfaces for analysis. The polished samples were coated with carbon. Microprobe analysis was performed by using a Cameca SX-100 electron probe microanalyzer with wavelength dispersive spectrometers. The characteristic X-rays generated by samples were analyzed by wavelength dispersive spectroscopy (WDS) to determine the compositions of samples. X-ray intensities of Eu, Zn, As, and Sn were compared with those of calibrated standards EuPO3, Zn (metal), GaAs, and Sn (metal) for quantitative analysis. At least 10 different points with a spot size of 1 μm were analyzed for each sample. The s a m p l e c o m p o s i t i o n w a s d e t e r m i n e d t o b e Eu1096(3)Zn399(2)Sn203(2)As1202(3) (Figure S2).

Energy Dispersive Spectroscopy (EDS). Single crystalline samples were enclosed in epoxy and polished to provide flat surfaces for analysis. Elemental mapping was performed using a FEI Scios dual-beam SEM/FIB microscope utilizing a window-less Oxford Instruments X-Max50 instrument, equipped with a 50 mm² silicon drift detector. The polished samples were coated with carbon, and Cu tape was added to minimize charging. Elemental mapping was employed to assess the spatial distribution of elements in the samples.

Quantum Chemical Calculations. Calculations of the band structure and density of states (DOS) for Eu₁₁Zn₄Sn₂As₁₂ were performed with the tight binding-linear muffin tin orbital-atomic sphere approximation TB-LMTO-ASA program package.³⁸ The experimentally determined unit cell dimensions and atomic coordinates at 90 K were used. The radial scalar-relativistic Dirac equation was solved to obtain the partial waves. Interstitial empty spheres were added to fill the interstitial space. The calculation was made for a grid of $8 \times 8 \times 4 \kappa$ points with 78κ points in the irreducible Brillouin zone. Integration over the Brillouin zone was performed by the tetrahedron method.³⁹ The basis set contained Eu (6s, 5d), As (4s, 4p), Zn (4s, 4p, 3d), and Sn (5s, 5p) with Eu (6p), As (4d), and Sn (5d, 4f) functions being downfolded, while 4f electrons of Eu were treated as core electrons. The electron localization function (ELF, η)^{40–42} was calculated with modules implemented within the TB-LMTO-ASA program package and evaluated on an adequately fine mesh of 0.06 Å. The topology of ELF and basins, which are bounded by zero-flux surfaces in the ELF gradient field, was analyzed using the program Basin implemented in DGrid version 4.6.43 The ParaView program was used for visualization of ELF isosurfaces and basins.

Magnetism. Magnetization measurements were performed in a Quantum Design Magnetic Properties Measurement System (MPMS) down to 2 K and up to 7 T; zero-field-cooled (ZFC) and field-cooled (FC) data were collected. The single crystals chosen for magnetic measurements were selected by morphology, and the unit cell was confirmed by single-crystal XRD. The single crystal presented below shows evidence of twinning of \sim 7° off the c axis, via XRD, aligned with the magnetic field parallel to the c axis.

Magnetoresistance. Magnetoresistance was measured in a Quantum Design Physical Property Measurement System (PPMS) from 0 to 9 T by the four-lead method using a current of 10 μ A. ø 25 μ m Pt leads were connected to a polished crystal, previously measured via EMPA and magnetic susceptibility. Silver epoxy was used to hold the wires in place and was cured under argon gas at 120 °C for 30 min. The crystal has a cross-sectional area of 1.40 \times 10⁻⁴ cm² and a voltage lead distance of 0.222 mm.

RESULTS AND DISCUSSION

Structural Description. On the basis of Laue symmetry and systematic absences, the structure of $\mathrm{Eu}_{11}\mathrm{Zn}_4\mathrm{Sn}_2\mathrm{As}_{12}$ was determined to be best described in a centrosymmetric monoclinic structure in the C2/c space group (No. 15) with 116 atoms per unit cell. For more details about the single-crystal X-ray diffraction experiment, see Table S1. The atomic coordinates in the unit cell are listed in Table S2. The $\mathrm{Eu}_{11}\mathrm{Zn}_4\mathrm{Sn}_2\mathrm{As}_{12}$ crystal structure contains 18 crystallographically unique positions comprised of eight Eu, two Sn, six As, and two Zn sites. All the atoms occupy the general position (8f Wyckoff positions) except Eu_5 , Eu_6 , and Eu_8 (at Eu_8 Cyckoff positions) and Eu_8 (at the Eu_8 Cyckoff position). The crystal structure of $\mathrm{Eu}_{11}\mathrm{Zn}_4\mathrm{Sn}_2\mathrm{As}_{12}$ projected along the a direction is shown in Figure 1. To examine the novelty of this structure,

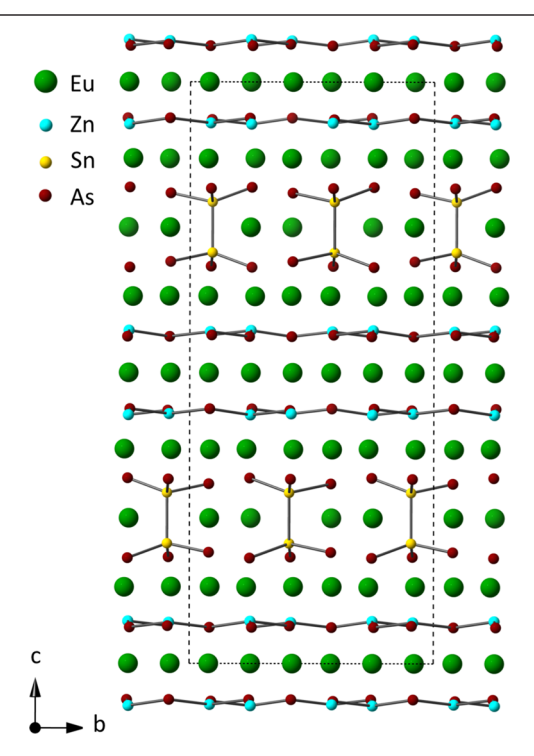


Figure 1. Crystal structure of Eu₁₁Zn₄Sn₂As₁₂ projected along the *a* axis

both the Wyckoff sequence $(f^{13}e^2d)$ and the Niggli cell of 7.56 7.56 31.31 92.42 92.42 119.926 calculated by the Visualization for Electronic and Structural Analysis (VESTA) program⁴⁵ were searched in the latest edition of the Inorganic Crystal Structure Database (ICSD). $Eu_{11}Zn_4Sn_2As_{12}$ is considered to be a new structure type because there were no compounds found with similar atomic arrangements. The electron microprobe analysis provided a composition of $Eu_{10.96(3)}Zn_{3.99(2)}Sn_{2.03(2)}As_{12.02(3)}$.

The $Eu_{11}Zn_4Sn_2As_{12}$ structure can be described as layers stacked in the *c* crystallographic direction (Figure 2). The

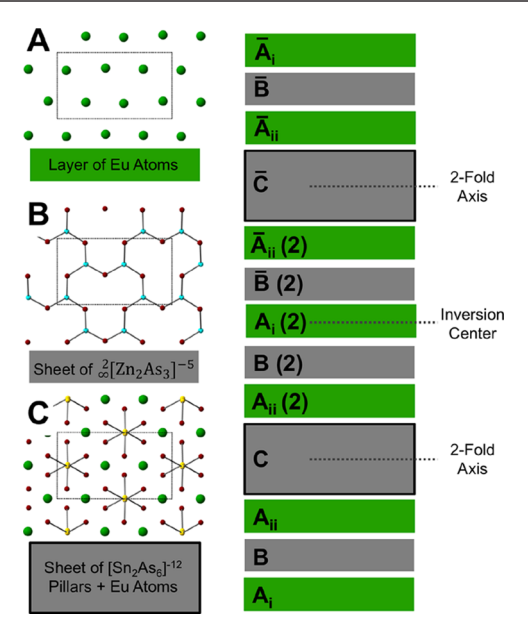


Figure 2. Three types of layers are shown in the a-b plane (left). Atoms and layers are color-coded according to Figure 1: Eu (A), sheets of $[Zn_2As_3]^{5-}$ (B), and layer of $[Sn_2As_6]^{12-}$ pillars (C). Stacking sequence of layers and their relationship through the position of the symmetry elements (right), where (2) stands for the equivalent layer produced by the 2-fold axis, the bar symbol denotes the inverted layer, and i or ii denotes the type of Eu monolayer.

layers can be classified on the basis of their chemical bonding into three types: layers of Eu cations (A), sheets of ${}^2_\infty[\mathrm{Zn_2As_3}]^{\mathrm{S-}}$ (B), and layers of $[\mathrm{Sn_2As_6}]^{\mathrm{12-}}$ pillars (C) (Figure 2, left). There are two types of Eu atom arrangements within the monolayer sheets shown by $\mathbf{A_i}$ and $\mathbf{A_{ii}}$ layers (the additional Eu atoms between the $\mathrm{Sn_2As_6}$ pillars, EuS and Eu6, are considered as part of layer C). Figure 2 (right) illustrates the 2-fold axis, located at $^1/_4c$ and passing through the central point of the Sn–Sn bond (layer C) while also passing through EuS and Eu6 sites (Figure 3a). The staggered

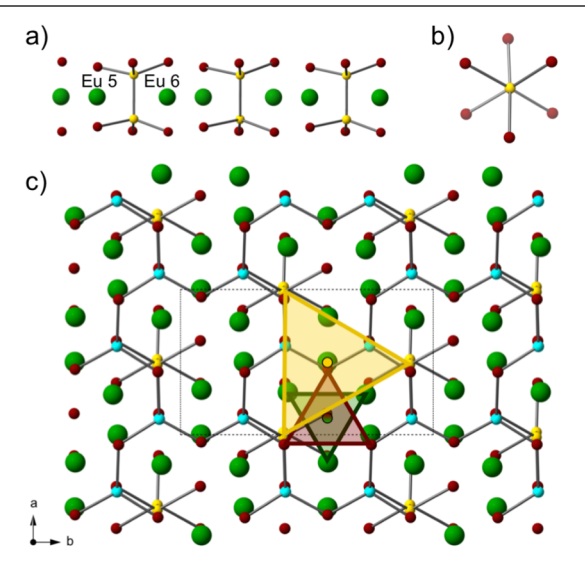


Figure 3. (a) Layer C with labeled Eu sites. (b) Newman projection along the Sn–Sn bond showing the staggered conformation. (c) Pseudo- C_3 symmetry of layers A (green), B (red), and C (yellow) of the structure. The center of each pseudo- C_3 is marked with the relevant color-filled circle.

conformation of the [Sn₂As₆]¹²⁻ pillar is shown in the Newman projection along the Sn-Sn bond (Figure 3b). The symmetrically equivalent layers are produced by the 2-fold symmetry element and indicated as $A_{ii}(2)-B(2)-A_{i}(2)$. The inversion center is located at the center of the $A_i(2)$ layer, and the symmetrically equivalent layers that resulted from the transformation through the inversion center are formed. Overall, the unit cell is made of $A_i-B-A_{ii}-C-A_{ii}(2)$ $B(2)-A_i(2)-\overline{B(2)}-\overline{A_{ii}(2)}-\overline{C}-\overline{A_{ii}}-\overline{B}-\overline{A_i}$ stacking sequence, where (2) stands for the equivalent layer produced by the 2-fold axis and the bar symbol denotes an inverted layer. All the layers show an approximate C_3 rotational axis parallel to the crystallographic c axis; however, atoms in the layers slightly deviate from perfect C_3 symmetry, and as a result, the structure does not contain trigonal symmetry. The pseudo- C_3 axes are not colinear as shown in Figure 3c. The Eu₁₁Zn₄Sn₂As₁₂ structure features two types of anionic arrangements: a $_{\infty}^{2}$ [Zn₂As₃]⁵⁻ two-dimensional (2D) net and a layer composed of isolated ethane-like [Sn₂As₆]¹²⁻. The [Sn₂As₆]¹²⁻ anions are separated by Eu cations filling the space between or within them to balance the charge. There is a small residual peak in the electron density map after the majority structure was determined that could be modeled with a stacking perturbation. This stacking perturbation can be found in approximately 1.5% of the structure. The perturbation can be described by the Sn1 site and the Eu5 site switching positions resulting in the C layer resembling the C layer (Figure 4). This

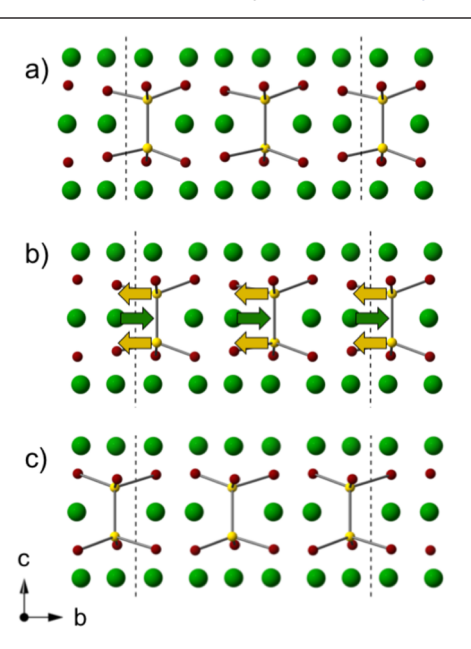


Figure 4. (a) Layer C as present in 98.5% of the structure. (b) Arrows illustrate the shifting direction of EuS and Sn1 labeled as Eu8 and Sn2 resulting in the stacking perturbation. (c) Layer C as present in 1.5% of the structure.

minor perturbation was observed in multiple crystals occurring at $\sim 1-2\%$ in each crystal. Ultimately, this effect does not change the composition of the material but results in a small disorder with respect to how the C layers are stacked relative to each other.

 $Eu_{11}Zn_4Sn_2As_{12}$ can be considered a Zintl phase and rationalized using the classic Zintl–Klemm electron counting rules. It can be best described in terms of discrete $\left[Sn_2As_6\right]^{12-}$ pillars with four-bond Sn^0 and one-bond As^{2-} , sheets of

 $_{\infty}^{2}$ [Zn₂As₃]⁵⁻ with two-bond As⁻ and three-bond Zn⁻, and isolated Eu²⁺ cations to represent a valence precise compound as the following calculation shows: Eu₁₁Zn₄Sn₂As₁₂ = 11Eu²⁺ × 2[Zn₂As₃]⁵⁻ + [Sn₂As₆]¹²⁻.

The ionic model would also suggest a valence precise compound. As the structure does not contain any As—As bond, arsenic atoms can be assigned their lowest oxidation number of -3. Considering that there is a homoatomic Sn—Sn bond in the $\mathrm{Sn}_2\mathrm{As}_6$ motif, it can be written as $\left[\mathrm{Sn}_2\right]^{6+}$, which means an oxidation state of +3 for each tin. Finally, the metal atoms can be assigned oxidation numbers of +2 for both europium and zinc. As a result, the compound can be considered as an electron precise compound as the number of electrons donated is equal to the number of electrons needed by the more electronegative elements.

The anionic motifs deserve particular attention in this structure. The $[Sn_2As_6]^{12-}$ isolated units are packed in a way that accommodates additional Eu ions between the Sn-Sn dumbbells (layer C). Upon careful examination of the dihedral angles of [Sn₂As₆]¹²⁻, a slight deviation from the ideal value of 60° (in the staggered conformation) is observed, ranging from 58.7° to 62.8°. Various anionic motifs have been reported for tin arsenide-based Zintl phases 46 such as isolated $[Sn_2As_6]^{10-}$ motifs formed through edge sharing of two SnAs₄ tetrahedra in Na_5SnAs_3 , 2D sheets of ${}_2^{\infty}[SnAs]^-$ made from Sn atoms coordinated by three arsenic atoms in $SrSn_2As_2$, ⁴⁸ isolated $[SnAs_4]^{8-}$ building blocks in $K_4Ba_2SnAs_4$, ⁴⁹ $[Sn_3As_6]^{6-}$ sheets made of connected Sn-centered tetrahedra in Ba₃Sn₄As₆, chains made by edge sharing of the [Sn₂As₆] units in Ba₃Sn₂As₄,⁵¹ and [Sn₂As₂]²⁻ layers made of connected Sn-centered trigonal pyramids in LiSn₂As₂.⁵² Among these compounds, Ba₃Sn₄As₆ and Ba₃Sn₂As₄ contain Sn-Sn bonds in the anionic motif. What makes $Eu_{11}Zn_4Sn_2As_{12}$ different from the reported tin-arsenic-based Zintl compounds described above is the isolated [Sn₂As₆]¹²⁻ motif containing the Sn-Sn dumbbells. The Sn-Sn distance in [Sn₂As₆]¹²⁻ of the Eu₁₁Zn₄Sn₂As₁₂ crystal structure is 2.7146 Å, which is similar to the length of the Sn-Sn bond in Ba₃Sn₂As₄ (2.7951 Å) and slightly shorter than that in Ba₃Sn₄As₆ (2.9021-2.8810 Å); both reported structures were collected at room temperature. The structure of Eu₁₁Zn₄Sn₂As₁₂ can also be compared with published structures of $Sr_{14}Sn_3As_{12}$ and $Eu_{14}Sn_3As_{12}$, featuring the same Sn₂As₆ ethane-like units.³¹ The structures of $A_{14}Sn_3As_{12}$ (A = Sr or Eu) can be understood according to the Zintl concept as containing the isolated [Sn₂As₆]¹²⁻² motif along with [SnAs₃]⁷⁻ trigonal pyramids and As³⁻ isolated anions. Compared to those observed in Eu₁₁Zn₄Sn₂As₁₂, the [Sn₂As₆]¹²⁻ motif is more distorted and the Sn-Sn bonds are also longer (2.8057 Å).

Layer **B** is shown in Figure 5 and can be described as a beehive-like sheet made from alternating Zn and As atoms with vacancies. The ordered "vacancies" shown as squares in Figure 5 (left) cause the As atoms to remain as two-coordinated centers, while Zn is a three-coordinated center with pseudotrigonal planar geometry shown in Figure 5 (right). This trigonal planar geometry at zinc centers is observed in compounds such as KZnAs⁵³ and Sr₂ZnAs₂. Standard Because of the absence of the vacancies in these compounds, the hexagonal symmetry is preserved and the As and Zn atoms both have a coordination number of 3. In Eu₁₁Zn₄Sn₂As₁₂, the beehive sheet is built of two crystallographically non-equivalent Zn atoms, Zn1 and Zn2, and three non-equivalent As atoms, As1—As3 (Table S2). In spite of the same geometrical environment

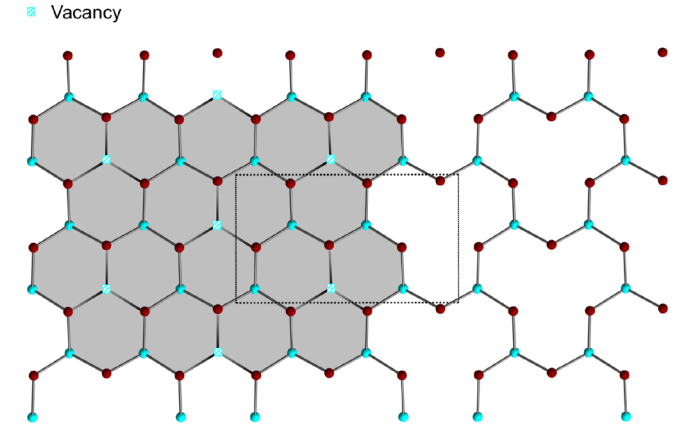


Figure 5. Ordered vacancies indicated by squares at the connection of each set of three arsenic atoms making up the beehive (left) and with larger openings as $\left[\mathrm{Zn_2As_3}\right]^{5-}$ with a pseudotrigonal topology (right). Atoms are color-coded according to Figure 1.

around both Zn1 and Zn2, Zn-As bonding distances are shorter for Zn1; the Zn-As bond ranges are 2.4873(2)-2.489(1) Å and 2.4922(2)-2.4984(1) Å for Zn1 and Zn2 sites, respectively (Table 1). These distances compare very

Table 1. Selected Bond Distances in the $Eu_{11}Zn_4Sn_2As_{12}$ Crystal Structure

atom pair	distance (Å)
Zn1-As1	2.488(1)
Zn1-As2	2.490(1)
Zn1-As3	2.488(1)
Zn2-As1	2.493(1)
Zn2-As2	2.493(1)
Zn2-As3	2.498(1)
Sn1-As4 ^a	2.6175(8)
Sn1-As5 ^a	2.6041(7)
Sn1-As6 ^a	2.5958(8)
Sn1-Sn1 ^a	2.7151(9)
Sn2-As4 ^b	2.69(3)
Sn2-As5 ^b	2.67(3)
Sn2-As6 ^b	2.48(3)
$Sn2-Sn2^b$	2.76(6)
a The 98.5% position. b The 1.5% position.	

well with Zn–As distances in other polar intermetallics such as REZn₂As₃⁵⁵ (2.447–2.673 Å), Ba₂Zn₃As₂O₂⁵⁶ (2.5787–3.4342 Å), BaZn₂As₂⁵⁷ (2.501–2.624 Å), Zn₃As₂⁵⁸ (2.390–2.880 Å), and A₂Zn₅As₄⁵⁹ (2.453–2.664 Å). However, in all of the aforementioned intermetallic compounds, zinc is surrounded by four arsenic atoms in the favorable tetrahedral geometry. Therefore, in the case of Eu₁₁Zn₄Sn₂As₁₂, the lattice must provide enough energy to stabilize the rare trigonal planar geometry for the zinc atom.

Quantum Chemical Calculations. According to the band structure calculation, $\operatorname{Eu}_{11}\operatorname{Zn}_4\operatorname{Sn}_2\operatorname{As}_{12}$ is a narrow gap $(E_g\sim 0.1\ \text{eV})$ semiconductor with zero density of states (DOS) at the Fermi level. As 4p and $\operatorname{Eu}\ 5d$ states have the largest contributions to the states at the top of the valence band (Figure 6). According to the band structure diagram (Figure S3), $\operatorname{Eu}_{11}\operatorname{Zn}_4\operatorname{Sn}_2\operatorname{As}_{12}$ is predicted to be an indirect semiconductor with a small indirect band gap of 0.1 eV as estimated from the energy difference between the Fermi level

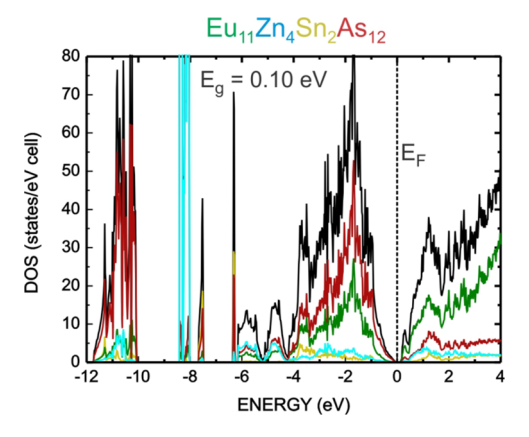


Figure 6. Total and partial density of states for $Eu_{11}Zn_4Sn_2As_{12}$. Contributions from Eu (green), Zn (blue), Sn (yellow), and As (dark red) states are color-coded.

and the bottom of the conduction band at the Z-point. The direct band gap is estimated to be larger, ~ 0.65 eV at the Γ point. The states between -12 and -10 eV consist mainly of As 4s and As 4p states, and states at around -8 eV correspond to Zn 3d localized contributions with some participation of Sn 5s and As 4s states. The peak right below 6 eV has contributions from Sn 5s and As 4p states. States between -6 eV and the Fermi level including the top of the valence band are composed of As 4p and Eu 5d states with smaller contributions from Sn 5p, Zn 4p, Zn 4s, Eu 6s, and Eu 6p states.

In the structure of $Eu_{11}Zn_4Sn_2As_{12}$, two types of arsenic atoms exist in a 1:1 ratio: those bonded to Zn atoms within the Zn_2As_3 layer (sites As1-As3) and those bonded to Sn atoms in the Sn_2As_6 fragment (sites As4-As6). The relative contributions from the 4p orbitals of two types of arsenic atoms to the top of the valence band are very similar and occur at the same energy span close to the Fermi level. Similarly, at the top of the valence band, the contributions from Eu states comprising the different Eu layers (shown in Figures 1 and 2) are alike when scaled to the same number of atoms. The Zn states at the Fermi level are predominantly Zn 4p states, while Zn 4s states are localized between -6 and -4 eV, and Zn 3d states at -8 eV and between -12 and -10 eV. Contributions of Zn1 and Zn2 to the state at the Fermi level are identical.

To further understand bonding in Eu₁₁Zn₄Sn₂As₁₂, the electron localization function (ELF, η) was calculated. ELF is a powerful tool for analyzing localized bonding and has been employed in a variety of compounds, including Eu-containing intermetallics and Zintl phases. 60-63 ELF analysis reveals the presence of localization domains corresponding to the single Sn-Sn bond within the Sn₂As₆ ethane-like unit (① in Figure 7) as well as localization domains corresponding to the Sn-As polar covalent bonding interaction (2 in Figure 7). The valence basin, which is defined by zero-flux surfaces in the ELF gradient, corresponding to attractor ① is disynaptic (i.e., has a common surface with two core Sn basins); thus, this attractor is attributed to the two-center Sn-Sn bond. The integration of electron density over this basin yields ~2.2e, which is in line with a single Sn–Sn bond. At moderate values of η (~0.6), localization domain ②, corresponding to the covalent Sn-As bonding interaction, can be clearly separated from localization domain 3, assigned to lone pairs on the As atom. This is consistent with the covalent Sn-As bond being strongly

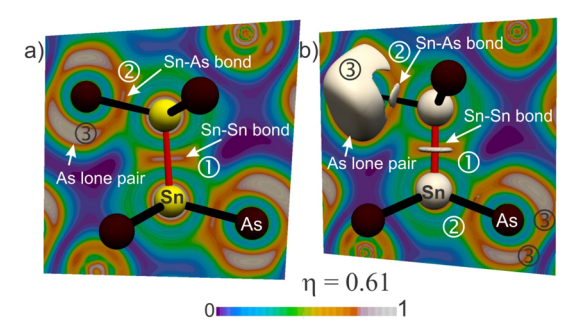


Figure 7. (a and b) 2D slices and (b) three-dimensional isosurfaces of the electron localization function (η) for the Sn_2As_6 unit. For the isosurfaces, an η value of 0.61 was used; the color scale bar is given at the bottom for the 2D slices. Sn is colored yellow, and As dark red. Localization domain ① corresponds to the two-center Sn–Sn bond. ② corresponds to the Sn–As covalent interaction. ③ corresponds to lone pairs on As.

polarized toward the more electronegative arsenic atom, which additionally bears lone pairs.

The bonding situation within the Zn₂As₃ layer is more complex (Figure 8). There are no distinct attractors

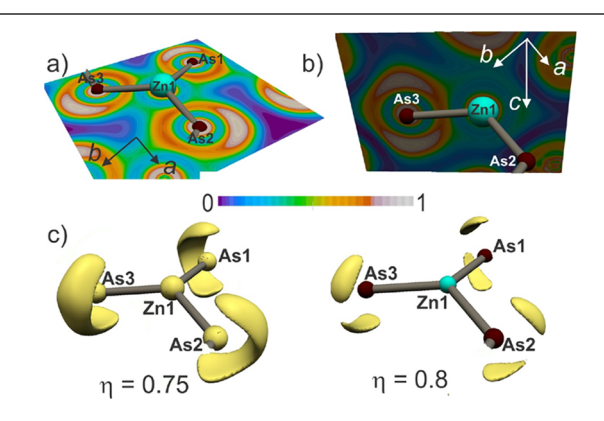


Figure 8. 2D slices of the electron localization function (η) for the Zn_2As_3 layer plotted in (a) the a-b plane or (b) orthogonal to the a-b plane. The color scale bar is given at the bottom for the 2D slices. (c) Three-dimensional isosurfaces of the electron localization function (η) with $\eta=0.75$ (left) or $\eta=0.8$ (right) for the Zn_2As_3 layer. Zn is colored blue, and As dark red.

corresponding to a two-center, two-electron Zn-As bond on the line connecting the two nuclei. Instead, unlike the spherical ELF distribution for a non-interacting atom, the valence shell of the arsenic atoms is distorted and at higher values of η becomes clearly separated into two lone pair-like localization domains. This suggests the strongly polarized interaction between As³⁻ anions and Zn²⁺ cations. Consistent with this description, the distribution of ELF around zinc atoms is spherical and nondistorted. Further insight was obtained from the topological partitioning of electron density using ELF, which yields basins of attractors that correspond to atomic cores, bonds, and electron lone pairs (not shown). In the case of an As atom surrounded by two Zn atoms, there are two valence polysynaptic basins; each of them has common surfaces with core basins of both adjacent Zn atoms as well as core basins of three neighboring Eu atoms. Thus, the bonding situation within the Zn₂As₃ layer can be described as the strongly polarized multicenter bonding between anioniclike As and Zn and the Eu cations. The absence of the distinct

attractors corresponding to the Zn–As two-center, two-electron covalent interaction, as opposed to the attractor found on the line between Sn and As within Sn₂As₆ unit, is in line with the larger electronegativity difference between Zn and As $(\chi_{As} - \chi_{Zn} = 2.18-1.65 = 0.53$; Pauling scale), as compared to that between Sn and As $(\chi_{As} - \chi_{Sn} = 2.18-1.96 = 0.22$; Pauling scale).

The ELF slices of two different Eu layers, A_i , which is sandwiched between two Zn_2As_3 layers, and A_{ii} , which is capped by a Zn_2As_3 layer from one side, and a layer consisting of Sn_2As_6 units from another side are shown in Figure S4. It is evident that in the case of Eu, the considerable shell structuring and deviation from the spherical symmetry occur with the maxima pointing toward As atoms, located above or below the Eu layer. This can be interpreted as additional covalent interactions involving europium and arsenic atoms, similar to Eu–Ge in EuGe₃, showing the limitation of the Zintl formalism in explaining this structure. ⁶⁴

Magnetic Properties. The magnetic susceptibility was measured on a single crystal from 2 to 300 K at 1 T (Figure 9).

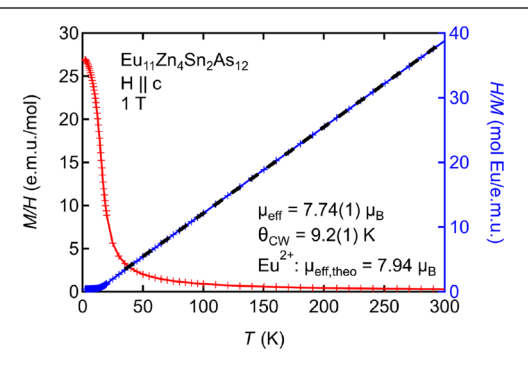


Figure 9. Molar magnetic susceptibility of $Eu_{11}Zn_4Sn_2As_{12}$ in an applied field of 0.1 T (red), the inverse susceptibility (blue), and its Curie–Weiss fit (black).

At this field, there was no difference in ZFC and FC data. Eu₁₁Zn₄Sn₂As₁₂ exhibits paramagnetic behavior above 15 K, and a fit of this portion of data utilizing the Curie-Weiss law $\chi(T) = C/(T - \theta)$, where χ is the molar susceptibility, C is the Curie constant ($C = N_A \mu_{eff}^2 / k_B$), and θ is the Curie–Weiss temperature, yields an effective moment of 7.74 (1) $\mu_{\rm B}$ per Eu atom, which is slightly lower but in reasonable agreement with the theoretical moment if all the Eu atoms were divalent Eu²⁺ cations (7.94 $\mu_{\rm B}$). The positive Curie–Weiss temperature of 9.2 (1) K indicates ferromagnetic coupling between Eu²⁺ spins, consistent with the observed ferromagnetic ordering below a T_c of 15 K. The magnetization versus field was measured at 2 K from 7 to -7 T (Figure 10). If the 11 Eu²⁺ cations in the structure were to fully saturate, the expected saturation moment is 77 $\mu_{\rm B}$. The data, below 6 T, show a saturation moment that is close to 49 $\mu_{\rm B}$, corresponding to seven Eu²⁺ cations. As the field is increased to 7 T, there is an increase in the saturation moment, suggesting that the magnetic moments on the four remaining Eu²⁺ ions are aligned antiparallel up to 5 T and become saturated at a higher field. It is not obvious which atoms to assign the strong coupling to as the distances between Eu²⁺ are similar, ranging from 4.035 to 4.437 Å.

The temperature dependence of the electrical resistivity at different applied fields is plotted in Figure 11. In the paramagnetic state, the resistivity increases upon cooling, which is consistent with semiconducting behavior and reaches

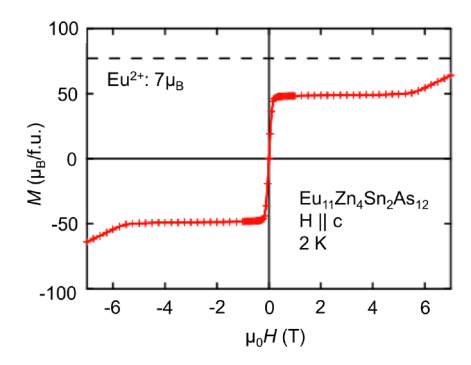


Figure 10. M vs H curve at 2 K of $Eu_{11}Zn_4Sn_2As_{12}$ with a partial saturation from 1 to 6 T and an additional increase from 6 to 7 T. The dotted black line indicates the expected saturation moment for 11 Eu^{2+} cations (77 μ_B).

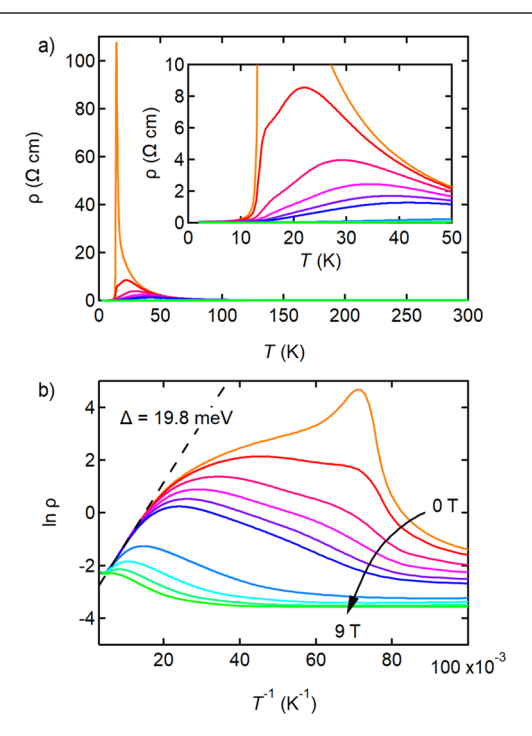


Figure 11. (a) Temperature-dependent electrical resistivity of Eu₁₁Zn₄Sn₂As₁₂ at applied magnetic fields of 0 (orange), 0.2, 0.4, 0.6, 0.8, 1, 3, 5, 7, and 9 T (green). The inset shows the temperature-dependent electrical resistivity of Eu₁₁Zn₄Sn₂As₁₂ in the temperature range of 2–50 K at different applied magnetic fields. (b) Ln ρ vs T^{-1} (100 × 10⁻³ K) for the same fields showing the fit to determine the activation energy.

a maximum at 14 K corresponding to the magnetic ordering. In Figure 11b, the dependence of $\ln \rho$ versus 1/T is shown. A linear behavior indicates that the resistivity can be described by a simple activation type relation $\rho \propto \exp(\Delta/k_{\rm B}T)$. Such behavior can be observed at 0 T in the range of 70–170 K with an activation energy Δ of 19.8 meV, leading to an estimated band gap value of 0.04 eV, in reasonable agreement with the result from band structure calculations (0.1 eV). In the ordered state, the resistivity abruptly decreases upon cooling below 14 K at 0 T. ${\rm Eu_{11}Zn_4Sn_2As_{12}}$ exhibits negative CMR (Figure 11, inset). The observed decrease in the electrical resistivity at the magnetic ordering or under applied magnetic field indicates that the ordering of the localized moments is accompanied by a delocalization of charge carriers. Figure 12 illustrates the

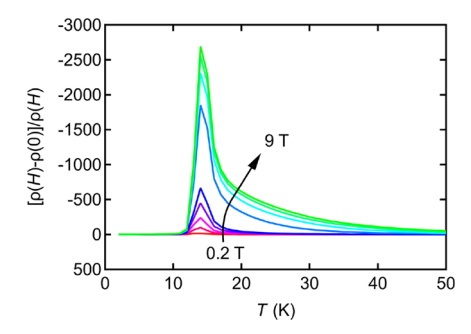


Figure 12. Magnetoresistance as a function of temperature at applied magnetic fields of 0.0, 0.2, 0.4, 0.6, 0.8, 1, 3, 5, 7, and 9 T.

magnetoresistance (MR), $\frac{|\rho(H)-\rho(0)|}{\rho(H)}$, as a function of temperature. A maximum negative MR is observed near the magnetic transition, consistent with the designation CMR. The decrease in resistance with applied field is calculated via $\frac{\rho(0)}{\rho(H)}$. At 9 T, we observe a 2690-fold decrease in resistivity at 14 K. Already at 0.2 T, a 15-fold decrease in resistivity is observed. The CMR effect is seen all the way to ~240 K (Figure S5), a temperature range much greater than those of other Eu-containing layered Zintl phases. For comparison, Eu₁₁Zn₄Sn₂As₁₂ has a 2311-fold decrease in CMR at 5 T. Eu₁₄MnSb₁₁ has an estimated 1.7-fold decrease, and the layered Eu/As-containing Zintl phase, EuIn₂As₂, exhibits an estimated 2.4-fold decrease in CMR at 5 T. The CMR for Eu₁₁Zn₄Sn₂As₁₂ is large compared to those of both Eu₁₄MnSb₁₁ and EuIn₂As₂. The effect of the magnetic field on the large negative magnetoresistance of Eu₁₁Zn₄Sn₂As₁₂ is summarized in Figure 13, with the inset

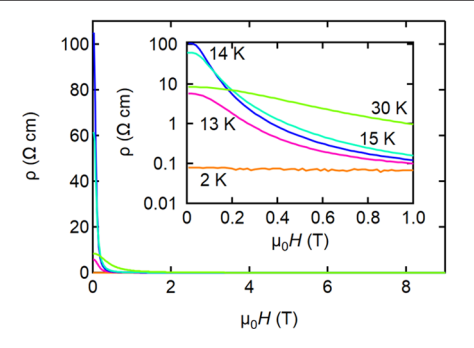


Figure 13. $\rho(H)$ as a function of the applied magnetic fields at the relevant temperatures. The inset shows low-field measurements.

showing the significant effect at low fields. As the magnetic field is applied, the electrical resistivity decreases by nearly 4 orders of magnitude at 14 K with an applied field of 1 T. A negative magnetoresistance of 7 orders of magnitude has been observed in $Nd_{1-x}Ca_xMnO_3$ as the system enters a ferromagnetic state, although it requires a much larger applied field of 5 T. ⁶⁵

CONCLUSIONS

Eu₁₁Zn₄Sn₂As₁₂ is the first example of a quaternary phase in the Eu–Zn–Sn–As system, a new member to the family of transition metal Zintl compounds. The crystal structure belongs to a new structure type consisting of alternately packed Eu layers between the anionic $[Zn_2As_3]^{2-}$ sheet and layers made of parallel isolated pillars of ethane-like $[Sn_2As_6]^{12-}$ species. To maintain the electron count in this

compound, all the Eu sites can be assumed as Eu²⁺ while Zn, Sn, and As sites can be assigned oxidation states of +2, +3, and -3, respectively. Electronic structure calculations predict Eu₁₁Zn₄Sn₂As₁₂ to be a narrow band gap semiconductor, consistent with the transport measurements. The chemical bonding evaluated by the calculation of ELF is consistent with a two-electron, two-center bond for Sn-Sn dumbbells, polar Sn-As covalent bonding within [Sn₂As₆]¹²⁻ units, while bonding within the Zn₂As₃ layer is best described as polarized multicenter interactions between anionic-like As and Zn and Eu cations. The measurements of magnetic properties confirm that all the Eu ions are Eu2+, consistent with the Zintl formalism. Eu₁₁Zn₄Sn₂As₁₂ is paramagnetic above 15 K with ferromagnetic ordering below 15 K. The magnetic ordering is accompanied by an anomalous decrease in resistivity. Eu₁₁Zn₄Sn₂As₁₂ exhibits a large negative CMR with a maximum reduction at 15 K, 3 orders of magnitude or 2689fold reduction at 9 T. Eu₁₁Zn₄Sn₂As₁₂ has unique magnetic properties, namely, the lack of saturation at 7 T, and the onset of magnetoresistance is exhibited at temperatures significantly higher than the ordering temperature. The magnetic properties will be evaluated further, employing Sr2+ to replace Eu2+ in Eu_{11-x}Sr_xZn₄Sn₂As₁₂, to unravel the unusual magnetic and electronic properties.

ASSOCIATED CONTENT

Supporting Information

The Supporting Information is available free of charge on the ACS Publications website at DOI: 10.1021/acs.chemmater.8b02749.

Crystal data, structure refinement, atomic coordinates, and equivalent isotropic displacement parameters for $Eu_{11}Zn_4Sn_2As_{12}$; band structure diagram for $Eu_{11}Zn_4Sn_2As_{12}$; 2D slices and three-dimensional isosurfaces of the electron localization function (η) for Eu layers A_i and A_{ii} ; and magnetoresistance data from 120 to 300 K (PDF)

Crystallographic information for Eu₁₁Zn₄Sn₂As₁₂ (CIF)

AUTHOR INFORMATION

Corresponding Author

*E-mail: smkauzlarich@ucdavis.edu.

ORCID 6

Julia V. Zaikina: 0000-0002-8755-1926 James C. Fettinger: 0000-0002-6428-4909 Susan M. Kauzlarich: 0000-0002-3627-237X

Present Address

§J.V.Z.: Department of Chemistry, Iowa State University, Ames, IA 50010.

Notes

The authors declare no competing financial interest.

ACKNOWLEDGMENTS

The authors thank Dr. Sarah Roeske and Nick Botto for assistance with microprobe analysis and Christopher J. Perez for his assistance with EDS mapping. The authors thank P. Klavins and K. Liu for useful discussions. The authors thank the National Science Foundation (Grant CHE-1531193) for the dual-source X-ray diffractometer. This research was funded by an Ernest E. Hill fellowship to N.K., GAANN fellowships to

J.A.C., and National Science Foundation Grants DMR-1405973 and DMR-1709382.

REFERENCES

- (1) Kimber, S. A. J.; Ling, C. D.; Morris, D. J. P.; Chemseddine, A.; Henry, P. F.; Argyriou, D. N. Interlayer Tuning of Electronic and Magnetic Properties in Honeycomb Ordered Ag₃LiRu₂O₆. *J. Mater. Chem.* **2010**, 20 (37), 8021–8025.
- (2) Zhao, L.-D.; Lo, S.-H.; Zhang, Y.; Sun, H.; Tan, G.; Uher, C.; Wolverton, C.; Dravid, V. P.; Kanatzidis, M. G. Ultralow Thermal Conductivity and High Thermoelectric Figure of Merit in SnSe Crystals. *Nature* **2014**, *508* (7496), 373–377.
- (3) Chen, Y. L.; Cui, Y. J.; Cheng, C. H.; Yang, Y.; Wang, L.; Li, Y. C.; Zhang, Y.; Zhao, Y. Low Temperature Preparation and Superconductivity of F-Doped SmFeAsO. *Phys. C* **2010**, *470* (20), 989–992.
- (4) Kawashima, Y.; Ichimura, K.; Katono, K.; Kurosawa, T.; Oda, M.; Tanda, S.; Kamihara, Y.; Hosono, H. STM/STS Study of the Superconducting Gap in SmFeAsO $_{1-x}F_x$. Solid State Commun. **2015**, 204, 33–36.
- (5) Stoyko, S. S.; Mar, A. Ternary Rare-Earth Arsenides $REZn_3As_3$ (RE = La-Nd, Sm) and $RECd_3As_3$ (RE = La-Pr). Inorg. Chem. 2011, 50 (21), 11152-11161.
- (6) Rotter, M.; Tegel, M.; Johrendt, D. Superconductivity at 38 K in the Iron Arsenide $(Ba_{1-x}K_x)Fe_2As_2$. *Phys. Rev. Lett.* **2008**, *101* (10), 107006.
- (7) Kauzlarich, S. M.; Brown, S. R.; Snyder, G. J. Zintl phases for thermoelectric devices. *Dalton Trans.* **2007**, 2099–2107.
- (8) Nomura, T.; Kim, S. W.; Kamihara, Y.; Hirano, M.; Sushko, P. V.; Kato, K.; Takata, M.; Shluger, A. L.; Hosono, H. Crystallographic Phase Transition and High- Tc Superconductivity in LaFeAsO:F. Supercond. Sci. Technol. 2008, 21 (12), 125028.
- (9) Brown, S. R.; Kauzlarich, S. M.; Gascoin, F.; Snyder, G. J. Yb₁₄MnSb₁₁: New High Efficiency Thermoelectric Material for Power Generation. *Chem. Mater.* **2006**, *18* (7), 1873–1877.
- (10) Bux, S. K.; Zevalkink, A.; Janka, O.; Uhl, D.; Kauzlarich, S. M.; Snyder, J. G.; Fleurial, J.-P. Glass-like Lattice Thermal Conductivity and High Thermoelectric Efficiency in Yb₉Mn_{4.2}Sb₉. *J. Mater. Chem. A* **2014**, 2 (1), 215–220.
- (11) Kazem, N.; Hurtado, A.; Klobes, B.; Hermann, R. P.; Kauzlarich, S. M. $Eu_9Cd_{4-x}CM_{2+x-y} \square_y Sb_9$: $Ca_9Mn_4Bi_9$ -Type Structure Stuffed with Coinage Metals (Cu, Ag, and Au) and the Challenges with Classical Valence Theory in Describing These Possible Zintl Phases. *Inorg. Chem.* **2015**, *54* (3), 850–859.
- (12) Kazem, N.; Hurtado, A.; Sui, F.; Ohno, S.; Zevalkink, A.; Snyder, J. G.; Kauzlarich, S. M. High Temperature Thermoelectric Properties of the Solid-Solution Zintl Phase Eu₁₁Cd_{6-x}Zn_xSb₁₂. *Chem. Mater.* **2015**, *27* (12), 4413–4421.
- (13) Zhang, H.; Fang, L.; Tang, M.-B.; Man, Z. Y.; Chen, H. H.; Yang, X. X.; Baitinger, M.; Grin, Y.; Zhao, J.-T. Thermoelectric Properties of $Yb_xEu_{1-x}Cd_2Sb_2$. *J. Chem. Phys.* **2010**, *133* (19), 194701.
- (14) Zhang, H.; Zhao, J.-T.; Grin, Y.; Wang, X.-J.; Tang, M.-B.; Man, Z.-Y.; Chen, H.-H.; Yang, X.-X. A New Type of Thermoelectric Material, EuZn₂Sb₂. *J. Chem. Phys.* **2008**, *129* (2008), 164713.
- (15) Mauger, A.; Godart, C. The Magnetic, Optical, and Transport Propertis of representative of a class of magnetic semiconductors: The europium chalcogenides. *Phys. Rep.* **1986**, *141*, 51–176.
- (16) Goforth, A. M.; Hope, H.; Condron, C. L.; Kauzlarich, S. M.; Jensen, N.; Klavins, P.; MaQuilon, S.; Fisk, Z. Magnetism and Negative Magnetoresistance of Two Magnetically Ordering, Rare-Earth-Containing Zintl Phases with a New Structure Type: EuGa₂Pn₂ (Pn = P, As). *Chem. Mater.* **2009**, 21 (19), 4480–4489.
- (17) Jiang, J.; Olmstead, M. M.; Kauzlarich, S. M.; Lee, H.-O.; Klavins, P.; Fisk, Z. Negative Magnetoresistance in a Magnetic Semiconducting Zintl Phase: Eu₃In₂P₄. *Inorg. Chem.* **2005**, 44, 5322–5327.
- (18) Kazem, N.; Kauzlarich, S. M. Chapter 288 Thermoelectric Properties of Zintl Antimonides. *Handbook on the Physics and Chemistry of Rare Earths* **2016**, *50*, 177–208.

(19) Shuai, J.; Mao, J.; Song, S.; Zhang, Q.; Chen, G.; Ren, Z. Recent progress and future challenges on thermoelectric Zinl materials. *Materials Today Physics* **2017**, *1*, 74–95.

- (20) MacDonald, A. H.; Schiffer, P.; Samarth, N. Ferromagnetic Semiconductors: Moving beyond (Ga,Mn)As. *Nat. Mater.* **2005**, *4* (3), 195–202.
- (21) Story, T.; Galazka, R. R.; Frankel, R. B.; Wolff, P. A. Carrier-Concentration-Induced Ferromagnetism in PbSnMnTe. *Phys. Rev. Lett.* **1986**, *56* (7), 777–779.
- (22) Chan, J. Y.; Klavins, P.; Shelton, R. N.; Webb, D. J.; Kauzlarich, S. M. Colossal Magnetoresistance in the Transition-Metal Compound Eu₁₄MnSb₁₁. *Chem. Mater.* **1997**, *9*, 3132–3135.
- (23) Wang, Y.; Darone, G. M.; Bobev, S. The new Zintl phases $Eu_{21}Cd_4Sb_{18}$ and $Eu_{21}Mn_4Sb_{18}$. J. Solid State Chem. **2016**, 238, 303–310
- (24) Suen, N.-T.; Wang, Y.; Bobev, S. Synthesis, Crystal structures, and physical properties of the new Zintl phases $A_{21}Zn_4Pn_{18}$ (A = Ca, Eu; Pn = As, Sb) Versatile arrangements of $[ZnPn_4]$ tetrahedra. *J. Solid State Chem.* **2015**, 227, 204–211.
- (25) Wang, J.; Xia, S.-Q.; Tao, X. T. $A_5Sn_2As_6$ (A = Sr, Eu). Synthesis, Crystal and Eletronic Structure, and Thermoelectric Properties. *Inorg. Chem.* **2012**, *51*, 5771–5778.
- (26) Ma, X.; Lu, J.; Whalen, J. B.; Latturner, S. E. Flux Growth and Magnetoresistance Behavior of Rare Earth Zintl Phase EuMgSn. *Inorg. Chem.* **2013**, *52*, 3342–3348.
- (27) Ernet, U.; Mullmann, R.; Mosel, B. D.; Eckert, H.; Pottgen, R.; Kotzyba, G. Magnetic hyperfine interactions in the Zintl phase EuZnSn. J. Mater. Chem. 1997, 7 (2), 255–257.
- (28) Stoyko, S. S.; Ramachandran, K. K.; Blanchard, P. E. R.; Rosmus, K. A.; Aitken, J. A.; Mar, A. Three series of quarernary rareearth transition-metal pnictides with CaAl₂Si₂-type structures: ReCuZnAs₂, REAgZnP₂, and REAgZnAs₂. *J. Solid State Chem.* **2014**, 213, 275–286.
- (29) Goforth, A. M.; Klavins, P.; Fettinger, J. C.; Kauzlarich, S. M. Magnetic Properties and Negative Colossal Magnetoresistance of the Rare Earth Zintl phase EuIn₂As₂. *Inorg. Chem.* **2008**, 47, 11048–11056.
- (30) Kim, H.; Olmstead, M. M.; Klavins, P.; Webb, D. J.; Kauzlarich, S. M. Structure, Magnetism, and Colossal Magnetoresistance (CMR) of the Ternery Transition Metal Solid Solution $Ca_{14-x}Eu_xMnSb_{11}$ (0 < x < 14). Chem. Mater. **2002**, 14, 3382–3390.
- (31) Liu, X.-C.; Pan, M.-Y.; Xia, S.-Q.; Tao, X.-T. Sr₁₄Sn₃As₁₂ and Eu₁₄Sn₃As₁₂: Enantiomorph-like Zintl Compounds. *Inorg. Chem.* **2015**, *54* (18), 8875–8877.
- (32) Liu, X.-C.; Pan, M.-Y.; Xia, S.-Q.; Tao, X.-T. $Sr_{14}Sn_3As_{12}$ and $Eu_{14}Sn_3As_{12}$: Enantiomorph-like Zintl Compounds. *Inorg. Chem.* **2015**, *54*, 8875–8877.
- (33) Ramirez, A. P. Colossal Magnetoresistance. J. Phys.: Condens. Matter 1997, 9, 8171–8199.
- (34) Kazem, N.; Xie, W.; Ohno, S.; Zevalkink, A.; Miller, G. J.; Snyder, G. J.; Kauzlarich, S. M. High Temperature Thermoelectric Properties of the Solid-Solution Zintl Phase $Eu_{11}Cd_6Sb_{12-x}As_x$ (x < 3). Chem. Mater. **2014**, 26 (3), 1393–1403.
- (35) Canfield, P. C.; Kong, T.; Kaluarachchi, S. U.; Jo, N. H. Use of frit-disc crucibles for routine and exploratory solution growth of single crystalline samples. *Philos. Mag.* **2016**, *96* (1), 84–92.
- (36) Sheldrick, G. M. A Short History of SHELX. Acta Crystallogr., Sect. A: Found. Crystallogr. 2008, 64 (1), 112–122.
- (37) Gelato, L. M.; Parthé, E. STRUCTURE TIDY a Computer Program to Standardize Crystal Structure Data. *J. Appl. Crystallogr.* **1987**, 20 (2), 139–143.
- (38) Jepsen, O.; Andersen, O. K. *The TB-LMTO-ASA Program*; Max-Planck-Institute fur Festokoperforschung: Stuttgart, Germany, 2000.
- (39) Blöchl, P. E.; Jepsen, O.; Andersen, O. K. Improved Tetrahedron Method for Brillouin-Zone Integrations. *Phys. Rev. B: Condens. Matter Mater. Phys.* **1994**, 49 (23), 16223–16233.
- (40) Becke, A. D.; Edgecombe, K. E. A Simple Measure of Electron Localization in Atomic and Molecular Systems. *J. Chem. Phys.* **1990**, 92 (9), 5397–5403.

(41) Savin, A.; Jepsen, O.; Flad, J.; Andersen, O. K.; Preuss, H.; von Schnering, H. G. Electron Localization in Solid-State Structures of the Elements: The Diamond Structure. *Angew. Chem., Int. Ed. Engl.* **1992**, 31 (2), 187–188.

- (42) Savin, A.; Nesper, R.; Wengert, S.; Fässler, T. F. ELF: The Electron Localization Function. *Angew. Chem., Int. Ed. Engl.* **1997**, *36* (17), 1808–1832.
- (43) Kohout, M. DGrid, version 4.6; 2011.
- (44) Baranov, A. I. Visualization Plugin for Paraview: Parallel Visualization Application, version 3.8.1.
- (45) Momma, K.; Izumi, F. VESTA 3 for Three-Dimensional Visualization of Crystal, Volumetric and Morphology Data. *J. Appl. Crystallogr.* **2011**, 44 (6), 1272–1276.
- (46) Liu, X.-C.; Lin, N.; Wang, J.; Pan, M.-Y.; Zhao, X.; Tao, X.-T.; Xia, S.-Q. Ba₁₃Si₆Sn₈As₂₂: A Quaternary Zintl Phase Containing Adamantane-Like [Si₄As₁₀] Clusters. *Inorg. Chem.* **2013**, 52 (20), 11836–11842.
- (47) Klein, J.; Eisenmann, B. Dimere Zintl-Anionen $[Sn_2As_6]^{10}$ Und $[Sn_2Sb_6]^{10}$ in Alkaliverbindungen. Z. Kristallogr. **1991**, 196, 213–229.
- (48) Eisenmann, B.; Klein, J. Zintl-Phasen Mit Schichtanionen: Darstellung Und Kristallstrukturen Der Isotypen Verbindungen SrSn₂As₂ Und Sr_{0.87}Ba_{0.13}Sn₂As₂ Sowie Eine Einkristallstrukturbestimmung von KSnSb. *Z. Anorg. Allg. Chem.* **1991**, 598 (1), 93–102.
- (49) Eisenmann, B.; Rößler, U. Pniktogenidostannate(IV) Mit Isolierten Tetraeder-Anionen: Neue Vertreter $(E1)_4(E2)_2[Sn(E15)_4]$ (mit E1 = Na, K; E2 = Ca, Sr, Ba; E15 = P, As, Sb, Bi) Vom Na₆[ZnO₄]-Typ Und Die Überstrukturvariante von K₄Sr₂[SnAs₄]. Z. Anorg. Allg. Chem. **2000**, 626 (6), 1373–1379.
- (50) Lam, R.; Mar, A. The Metallic Zintl Phase Ba₃Sn₄As₆. Solid State Sci. **2001**, 3 (4), 503–512.
- (51) Eisenmann, B.; Jordan, H.; Schafer, H. Notizen: Ba₃Sn₂As₄, eine neue Zintlphase mit Kettenstruktur/ On Ba₃Sn₂As₄, a New Zintl Phase with Chain Structure. *Z. Naturforsch., B: J. Chem. Sci.* **1984**, 39 (8), 1151–1153.
- (52) Lee, K.; Kaseman, D.; Sen, S.; Hung, I.; Gan, Z.; Gerke, B.; Pöttgen, R.; Feygenson, M.; Neuefeind, J.; Lebedev, O. I.; Kovnir, K. Intricate Short-Range Ordering and Strongly Anisotropic Transport Properties of Li_{1-x}Sn_{2+x}As₂. *J. Am. Chem. Soc.* **2015**, *137* (10), 3622–3630.
- (53) Vogel, R.; Schuster, H.-U. KHgAs (Sb) Und KZnAs-Ternäre Verbindungen Mit Modifizierter Ni₂In-Struktur. *Z. Naturforsch., B: J. Chem. Sci.* **1980**, 35, 114–116.
- (54) Wilson, D. K.; Saparov, B.; Bobev, S. Synthesis, Crystal Structures and Properties of the Zintl Phases Sr_2ZnP_2 , Sr_2ZnAs_2 , A_2ZnSb_2 and A_2ZnBi_2 (A = Sr and Eu). Z. Anorg. Allg. Chem. **2011**, 637 (13), 2018–2025.
- (55) Lin, X.; Stoyko, S. S.; Mar, A. Ternary Rare-Earth Zinc Arsenides {REZn₂As₃} (RE = La-Pr) Containing Defect Fluorite-Type Slabs. *J. Solid State Chem.* **2013**, *199*, 189–195.
- (56) Brock, S. L.; Kauzlarich, S. M. $A_2Zn_3As_2O_2$ (A = Ba, Sr): A Rare Example of Square Planar Zinc. *Inorg. Chem.* **1994**, 33 (11), 2491–2492.
- (57) Klufers, P.; Mewis, A. Zur Struktur Der Verbindungen $BaZn_2P_2$ Und $BaZn_2As_2$ /The Crystal Structure of $BaZn_2P_2$ and $BaZn_2As_2$ Z. Naturforsch., B: J. Chem. Sci. 1978, 33 (2), 151–155.
- (58) Pietraszko, A.; Lukaszewicz, K. The crystal structure of zinc arsenide polymorphic modifications alpha-Zn₃As₂ and alpha'-Zn₃As₂. *Bull. Acad. Pol. Sci., Ser. Sci. Chim.* **1976**, 24 (6), 459–461.
- (59) Stoyko, S. S.; Khatun, M.; Mar, A. Ternary Arsenides $A_2Zn_2As_3$ (A = Sr, Eu) and Their Stuffed Derivatives $A_2Ag_2ZnAs_3$. *Inorg. Chem.* **2012**, 51 (4), 2621–2628.
- (60) Kazem, N.; Zaikina, J. V.; Ohno, S.; Snyder, G. J.; Kauzlarich, S. M. Coinage-Metal-Stuffed $Eu_9Cd_4Sb_9$: Metallic Compounds with Anomalous Low Thermal Conductivities. *Chem. Mater.* **2015**, 27 (21), 7508–751.
- (61) Sichevych, O.; Kohout, M.; Schnelle, W.; Borrmann, H.; Cardoso-Gil, R.; Schmidt, M.; Burkhardt, U.; Grin, Y. $EuTM_2Ga_8$ (TM = Co, Rh, Ir) A Contribution to the Chemistry of the $CeFe_2Al_8$ -Type Compounds. *Inorg. Chem.* **2009**, *48* (13), 6261–6270.

(62) Wang, S.; Yang, J.; Wu, L.; Wei, P.; Yang, J.; Zhang, W.; Grin, Y. Anisotropic Multicenter Bonding and High Thermoelectric Performance in Electron-Poor CdSb. *Chem. Mater.* **2015**, 27 (3), 1071–1081.

- (63) Wang, X. J.; Tang, M. B.; Chen, H. H.; Yang, X. X.; Zhao, J. T.; Burkhardt, U.; Grin, Y. Synthesis and High Thermoelectric Efficiency of Zintl Phase YbCd_{2-x}Zn_xSb₂. *Appl. Phys. Lett.* **2009**, 94 (9), 092106.
- (64) Castillo, R.; Baranov, A. I.; Burkhardt, U.; Grin, Y.; Schwarz, U. Triangular Ge₃ Units in a New Modification of EuGe₃. *Z. Anorg. Allg. Chem.* **2015**, 641 (2), 355–361.
- (65) Liu, K.; Wu, X. W.; Ahn, K. H.; Sulchek, T.; Chien, C. L.; Xiao, J. Q. Charge ordering and magnetoresistance in $Nd_{1-x}Ca_xMnO_3$ due to reduced double exchange. *Phys. Rev. B: Condens. Matter Mater. Phys.* **1996**, 54 (5), 3007–3010.